

Multiphasic Collagen Scaffolds for Engineered Tissue Interfaces

Alexander J. Lausch, Lester C. Chong, Hasan Uludag, and Eli D. Sone*

Hard–soft tissue interfaces pose unique challenges for regeneration due to architectural, mechanical, and compositional changes between tissues, which are difficult to incorporate into tissue engineering scaffolds. Multiphasic scaffolds are needed to better mimic structural and chemical changes through the incorporation of layers with distinct properties. A particular challenge in the production of multilayered constructs is achieving cohesion between layers. Herein, a novel system is developed, which combines sequential collagen self-assembly and diffusion gradients in mineralization to produce multiphasic collagen scaffolds that have intrinsic connectivity and porosity between layers, with no need for adhesives or heat treatments. The scaffolds incorporate mineralized layers, wherein the mineralized collagen fibrils have intrafibrillar oriented mineral resembling bone, alongside unmineralized layers. The interface between mineralized and unmineralized layers is sharp and well defined, with nonmineralized fibrils inserting into the mineralized layer to create mechanical interlock and cohesion. Inspired by the complex architecture of the periodontal attachment apparatus (bone–ligament–cementum), it is demonstrated that the model system can be applied to the development of a trilayered collagen scaffold with potential for periodontal regeneration.

1. Introduction

Biological tissue interfaces allow for a functional transition or attachment between distinct tissues. In connective tissues these interfaces can occur between hard and soft tissues such as in osteochondral zones,^[1–7] tendon entheses,^[8] and ligament insertions.^[9,10] Restoring connectivity at tissue interfaces is often necessary following injury or disease. Tissue engineering of such interfaces is particularly difficult due to differences in tissue architecture, cell population, and mechanical properties. Multiphasic scaffolds that exhibit inherent changes in architecture

(pore size, material, etc.) and/or composition (cells, molecules, etc.) either over a gradient or by compartmentalization have been explored and these studies have been reviewed comprehensively.^[6,11–16] In particular, multiphasic scaffolds are well suited for the regeneration of periodontal tissues (bone–ligament–cementum), wherein tissue-specific layers can be constructed and surgically implanted to guide regeneration and tooth reattachment.^[17–22]

A key requirement of a multilayered scaffold is strong cohesion between the specific layers,^[6] preventing delamination, while maintaining interconnectivity to allow for cell migration and diffusion. Most multiphasic scaffolds fail to address this issue. Biocompatible adhesives such as fibrin glue can be used^[2,5,23]; however, they almost certainly reduce connectivity and their degradation in vivo can result in delamination. Heat pressing can be used with some synthetic polymers, but is not compatible with cell delivery and


cells must be seeded after assembly.^[21,24] Electrospun layers of collagen attached with cell sheet technology have been developed for osteochondral applications,^[3] but this approach is limited by dimensional restrictions. 3D-printing methods can also result in adhesion between layers; however, even the best printers are limited by their resolution and are not yet able to print features in the range of typical extracellular matrix components (e.g., collagen fibrils ≈100 nm).^[18,20,22]

Fibrillar collagen is the main protein constituent of almost every connective tissue and has been shown to induce osteogenic differentiation in bone marrow cells through integrin interactions.^[25–27] Not surprisingly, multiphasic collagen scaffolds have been explored previously for osteochondral engineering.^[1,2,4,7,10,28] However, most collagen-based scaffolds for bone/cartilage regeneration do not contain fibrillar collagen,^[1,28–33] and instead use lyophilized collagen solutions (or slurries containing hydroxyapatite (HA) powders or glycosaminoglycans) to create scaffolds. The resulting structure, though porous, does not resemble native collagen.

The incorporation of hydroxyapatite into collagen-based scaffolds improves mechanical properties^[34–36] and further encourages bone formation.^[37,38] In vivo, the collagen fibrils of mineralized tissues are fully infiltrated with aligned platelets of hydroxyapatite. Polyelectrolytes such as polyaspartic acid (pAsp),^[39–42] polyacrylic acid,^[43] and poly(allylamine)^[44] have

Dr. A. J. Lausch, L. C. Chong, Prof. E. D. Sone
Institute of Biomaterials and Biomedical Engineering
Department of Materials Science and Engineering
Faculty of Dentistry
University of Toronto
Toronto, ON M5S 3G9, Canada
E-mail: eli.sone@utoronto.ca

Prof. H. Uludag
Chemical and Materials Engineering
University of Alberta
Edmonton, AB T6G 1H9, Canada

 The ORCID identification number(s) for the author(s) of this article can be found under <https://doi.org/10.1002/adfm.201804730>.

DOI: 10.1002/adfm.201804730

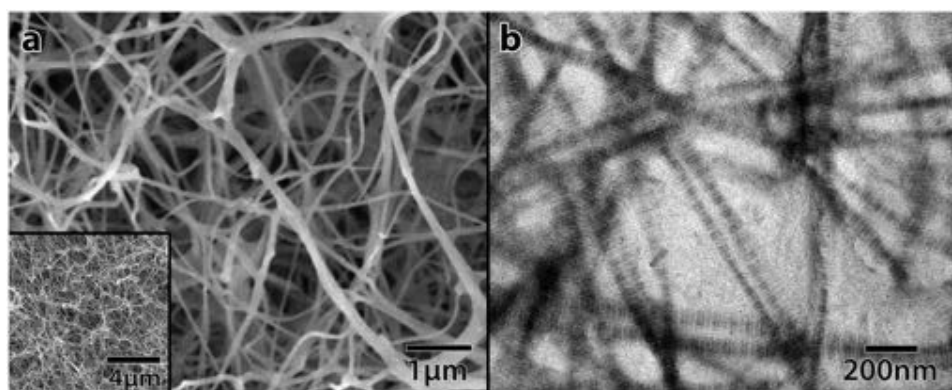


Figure 1. Fibrillar, self-assembled collagen scaffolds. a) SEM of a lyophilized collagen scaffold showing well defined fibrils and 2–6 μm pore size. The inset shows lower magnification image to show porosity and homogeneity. b) TEM of a collagen scaffold stained with UA showing characteristic banding pattern. Fibrils are ≈ 100 – 200 nm in diameter.

been shown to direct intrafibrillar mineralization *in vitro*. Such biomimetic mineralization pathways are now being explored in the context of scaffolds for bone tissue engineering. Cell culture studies have demonstrated clear benefits of biomimetic mineralized collagen. For example, cells cultured on intrafibrillar mineralized collagen exhibit increased proliferation and osteoblastic differentiation over traditionally mineralized (extrafibrillar mineral), and unmineralized collagen.^[45,46] Similarly, Ye et al. demonstrated that biomimetic mineralized collagen (intrafibrillar and extrafibrillar mineral) promotes cell adhesion, proliferation, and differentiation of human umbilical cord stem cells.^[47] Despite the clear benefit of biomimetic mineralized collagen for bone (or other mineralized tissues) regeneration, no studies have incorporated intrafibrillar mineralization into multilayered scaffolds. Moreover, few studies have investigated the macroscale mineral distribution in *in vitro* mineralized scaffolds, likely due to the difficulty in creating fully mineralized scaffolds; diffusional limitations often result in significant surface mineralization, inhibiting bulk mineralization,^[48–50] which is a limitation for bone regeneration. Similarly, the effect of fixation has not been thoroughly investigated, which is important for scaffold stabilization as it enhances mineralization^[36] and reduces antigenicity.^[51]

Here we show the development of multiphasic collagen scaffolds for the regeneration of hard–soft tissue interfaces. Our scaffolds are produced using an in-well mineralization system that allows us to create interconnected, mineralized–unmineralized layers and have spatial control over mineralization using a combination of diffusion and layering. We show that our mineralized collagen closely resembles native mineralized tissues and that our system results in inherent cohesion between layers. As a proof of principle, we demonstrate a scaffold designed to mimic the periodontium—the set of tissues which anchors the tooth (bone, ligament, and cementum).

2. Results

2.1. Collagen Gelation and Mineralization

To create porous collagen scaffolds, we casted gels of acid-soluble, type I collagen from rat tail tendon, via ammonia vapor diffusion,

in cylindrical molds ($d = 7$ mm; $h = 10$ mm). pH-mediated self-assembly results in the formation of fibrillar collagen gels with customizable size and shape. Collagen gels were crosslinked, washed, frozen, and lyophilized for scanning electron microscopic (SEM) analysis. From **Figure 1**, it is immediately clear that the scaffolds are entirely fibrillar with fibril diameters (70–100 nm) in the lower range for rat tail tendon.^[52] The scaffold is sponge-like with a high degree of porosity and interconnectivity (Figure 1a) with pore sizes ranging from 2 to 6 μm . Uranyl acetate (UA) staining of the collagen gels resembles that of native collagenous tissues and other reconstituted collagen models.^[40,53]

To mineralize collagen gels we used a metastable solution of calcium and phosphate containing pAsp.^[41,42,54] The mineralization solution itself does not precipitate homogeneously within experimental parameters. Gels were removed from molds, immersed in mineralization solution at 37 °C with stirring. Using backscattered electron-SEM (BSE) and transmission electron microscopy (TEM) we are able to characterize both the distribution of mineral in our scaffolds, and collagen–mineral relationships. **Figure 2a** shows BSE-SEM imaging of a mineralized collagen gel. By 2 d we can see collagen fibrils beginning to mineralize from random locations. Collagen fibrils appear to swell in diameter and straighten as they mineralize. This has been seen in naturally mineralizing turkey tendon^[55] and mouse cementum^[56] as well as in an *in vitro* model of collagen biomineralization.^[40] The mineral is closely associated with the fibrils and is not found in the interfibrillar space (between fibrils). By TEM (Figure 2b) the mineral appears to be entirely collagen-associated. Electron diffraction shows that the mineral phase is HA and that the *c*-axis of the HA crystals is oriented with the long axis of the collagen fibril. The preferred orientation of crystals is seen by the presence of the [002] and [004] diffraction arcs. These features suggest that the mineral is intrafibrillar, as has been observed in electron tomography studies of mineralized collagen fibrils from similar solutions.^[40] These results show that collagen structure and collagen–mineral relationships of our mineralized scaffolds closely resemble native mineralized collagen.

To quantify the amount of mineral present and compare the effect of fixation on mineralization rates, we used thermogravimetric analysis (TGA). **Figure 3** shows TGA data for scaffolds fixed with glutaraldehyde or EDC and mineralized for 2–6 d in

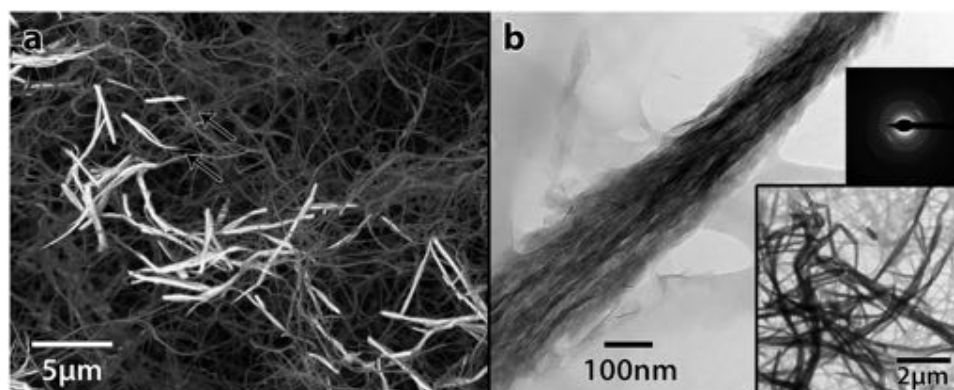


Figure 2. Electron microscopic images of collagen scaffolds mineralized for 2 d. a) BSE image revealing mineralized fibrils. The bright contrast seen in specific fibrils is indicative of mineralization due to increased backscatter signal from the presence of hydroxyapatite. Unmineralized fibrils appear dull grey. b) TEM shows individual crystals within the collagen fibril. Selected area diffraction reveals oriented crystals of hydroxyapatite with the *c*-axis aligned with the long axis of the collagen fibril. The inset shows lower magnification to show intrafibrillar mineralization in many fibrils.

a stirred beaker of mineralization solution. Initially EDC-fixed scaffolds mineralized faster than scaffolds fixed with glutaraldehyde. However, after 4 d the amount of mineral is no longer significantly different between the two fixation methods. By 6 d, all samples are 50–55 wt% mineral, which is similar to native bone (67 wt%)^[57] and similar mineralized scaffolds.^[36]

We investigated possible cytotoxicity of glutaraldehyde fixation by comparing cell viability of rat bone chip cells cultured on unfixed and glutaraldehyde-fixed scaffolds using a 3-(4,5-dimethylthiazol-2-yl)-2,5-diphenyltetrazolium bromide assay. We observed no cytotoxicity as a result of fixation over 7 d culture, using cells from two separate animals (see Figure S1, Supporting Information).

2.2. In-Well Mineralization System

We developed an in-well mineralization system to achieve better spatial control over mineralization by restricting the diffusion

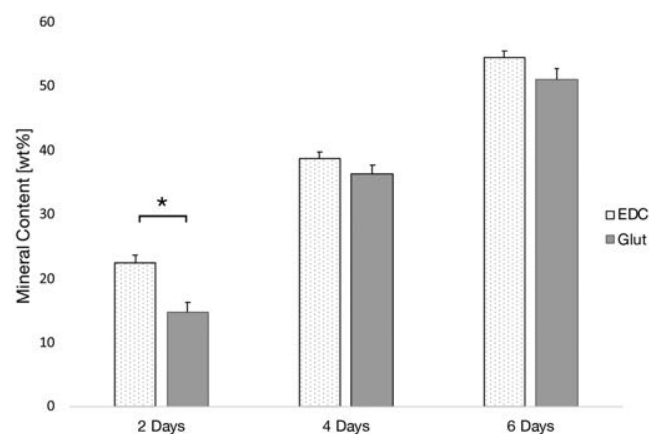


Figure 3. Thermogravimetric analysis of EDC or glutaraldehyde fixed scaffolds mineralized in CaP1 for 2, 4, and 6 d shows that after 4 d the mineral content between scaffolds is no longer significantly different. Error bars show standard deviation ($n = 3$), and asterisk indicates significance. Mineral content for all conditions is significantly different except between EDC and Glut at 4 and 6 d.

of mineralizing solution to one dimension (top-down). Additionally, this allows us to more easily characterize changes in mineral distribution over time. Gels were cast, mineralized, and lyophilized in 24-well plates. After lyophilization we removed scaffolds from their wells and imaged the tops and cross-sections by BSE-SEM to characterize mineral distribution. **Figure 4a** shows evidence of a surface layer, which is more mineralized than the bulk. This hypermineralized layer appears to be $\approx 120 \mu\text{m}$ thick by 6 d. The interface between the hypermineralized layer and the bulk of the scaffold is sharp and well defined. Clearly, all fibrils in this layer are fully mineralized; however, the mineral remains intrafibrillar and there is no visible interfibrillar mineral (Figure 4a, inset). Energy dispersive X-ray spectroscopy (EDX) shows that there is a Ca:P ratio of 1.74 (at 10 d; Figure S3, Supporting Information), similar to stoichiometric HA (1.67). Figure 4b shows the middle of the scaffold (bulk) where mineralization seems to be occurring in specific fibrils but with a homogenous distribution. Surprisingly, we do not observe a gradient of mineralization. In fact, the bottom layer has similar amounts of mineral at this time point to the cross-section seen in Figure 4b (not shown). However, it is possible that in thicker scaffolds a gradient would be present in the bulk.

2.3. Characterization of the Hypermineralized Layer

To characterize the formation of a hypermineralized layer we looked at cross-sections of mineralizing collagen gels (in 24-well plates) over time and analyzed them by SEM. We note that mineralization is slower in smaller wells (96-well plates) due to smaller volumes and decreased agitation (due to surface tension). **Figure 5a** shows that at 4 d of mineralization almost all mineral is intrafibrillar and mineralized fibrils appear smooth with no visible mineral growing on (extrafibrillar) or between (interfibrillar) fibrils. Indeed, BSE imaging shows that all fibrils are fully mineralized on the top surface (Figure 5a, inset). By 6 d we start to see a spiky morphology on the fibril surfaces (Figure 5c). This extrafibrillar mineralization increases by 14 d; however, porosity is unaffected, and we see no evidence of

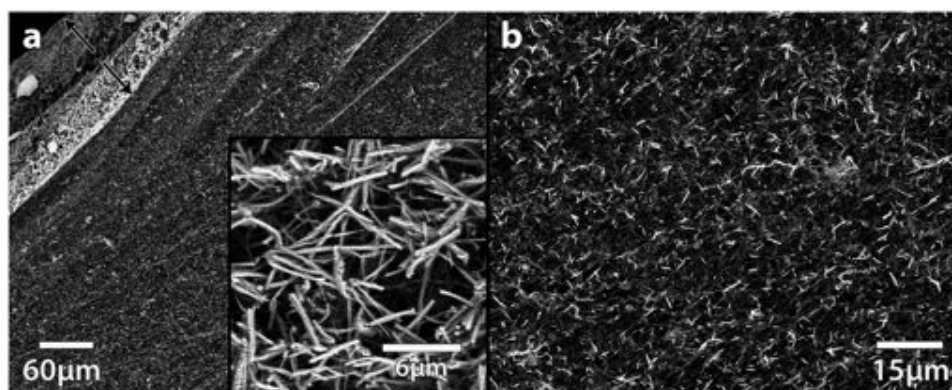


Figure 4. BSE micrographs of collagen scaffolds mineralized in 24-well plates for 6 d (cross sections). a) An overview of the cross-section revealing a hypermineralized layer on the surface (top left). Arrows delineate the borders of the hypermineralized layer, which is $\approx 120\ \mu\text{m}$ thick. The inset shows the top surface of the hypermineralized layer that is fully mineralized. We note that the upper (top left) half of this layer appears less mineralized than the lower half. This is an artifact of sample preparation where the fracture plane is not exactly flat; the different angle results in less signal in the top half. High magnification images confirm this (not shown). b) Higher magnification of the bulk (middle of scaffold), which is significantly less mineralized than the hypermineralized layer. The mineralization is homogenous, and we do not see evidence of a gradient.

interfibrillar mineral (mineral forming between fibrils). We also see that the thickness of the hypermineralized layer increases with time. At 4 d, the layer is $\approx 60\ \mu\text{m}$ thick, increasing to $\approx 500\ \mu\text{m}$ by 6 d and greater than $700\ \mu\text{m}$ at 14 d. We note that the thickness of the layer is greater at the meniscus, due to greater surface area for diffusion. At all time points the interface between the hypermineralized layer and the bulk is sharp and well defined. These results show that the hypermineralized layer increases in thickness over time but at all time points mineralization remains intrafibrillar and/or extrafibrillar, with no mineral forming between fibrils.

2.4. Multiphasic Scaffold

Our well-plate system allows us to manufacture multilayered scaffolds, with control over spatial distribution of the mineralized collagen, as well as the thickness and number of layers. After gelation and fixation, additional layers can be incorporated by gelling acid soluble collagen on top of the gel. **Figure 6** shows a hydrated scaffold after gelation of a second layer. Alcian blue stain was added to acid soluble collagen before gelation in order to make the interface visible. The connection between layers does not fracture preferentially along the interface when compressed with a scoopula, indicating that the mechanical properties are similar throughout the scaffold regardless of the incorporation of added layers.

To create biphasic scaffolds, acid soluble collagen was gelled on a premineralized scaffold. We characterized the interface using SEM analysis of scaffold cross-sections. **Figure 7** shows a biphasic scaffold consisting of a 6 d mineralized layer and an unmineralized layer. Clearly the interface between the two layers is very sharp, as seen in the hydrated scaffold seen in **Figure 6**. There appears to be little to no dissolution of the mineral phase through the addition of the second layer. Most importantly, the higher magnification seen in **Figure 7c** shows unmineralized fibrils of the second layer interdigitating with the mineralized layer, creating mechanical interlock. No mineralized fibrils appear in the unmineralized layer (**Figure 7d**).

These results show that through the addition of a second layer we can create continuous, interconnected multiphasic scaffolds incorporating multiple phases. We note that the apparent change in pore size in the unmineralized layer is an artifact of lyophilization, where the nonmineralized layer is more prone to collapse.

2.5. Triphasic Scaffold for Periodontal Regeneration

The periodontium is a unique set of connective tissues and is comprised of bone, periodontal ligament (PDL), and cementum. To create a scaffold that resembles the architecture of the periodontium we incorporated a third layer by taking advantage of the formation of a hypermineralized layer. After incorporating a second unmineralized layer (as seen in **Figure 7**), the top, unmineralized layer was mineralized for a short period of time. **Figure 8** shows BSE imaging of the interface between the mineralized (bone) and unmineralized (PDL) compartments. The bone compartment was mineralized for 10 d, and the third layer was mineralized for 4 d. The inset shows the top surface of unmineralized compartment, where all collagen fibrils on the surface have mineralized. With the exception of this thin surface layer no mineralization is seen in the PDL layer (not shown). We note that the hypermineralized layer of the bone compartment is thinner than expected by 10 d as is compared in **Figure 7**. However, as previously stated, mineralization in 96-well plates is slightly slower due to decreased agitation and it is possible that some dissolution occurred due to the incorporation of the second layer. The intrafibrillar mineralization seen in the bone compartment continues through the entire thickness of the compartment ($\approx 1\ \text{mm}$, not shown).

3. Discussion

We show the development of biomimetic, stratified, collagen scaffolds for the regeneration of hard–soft tissue

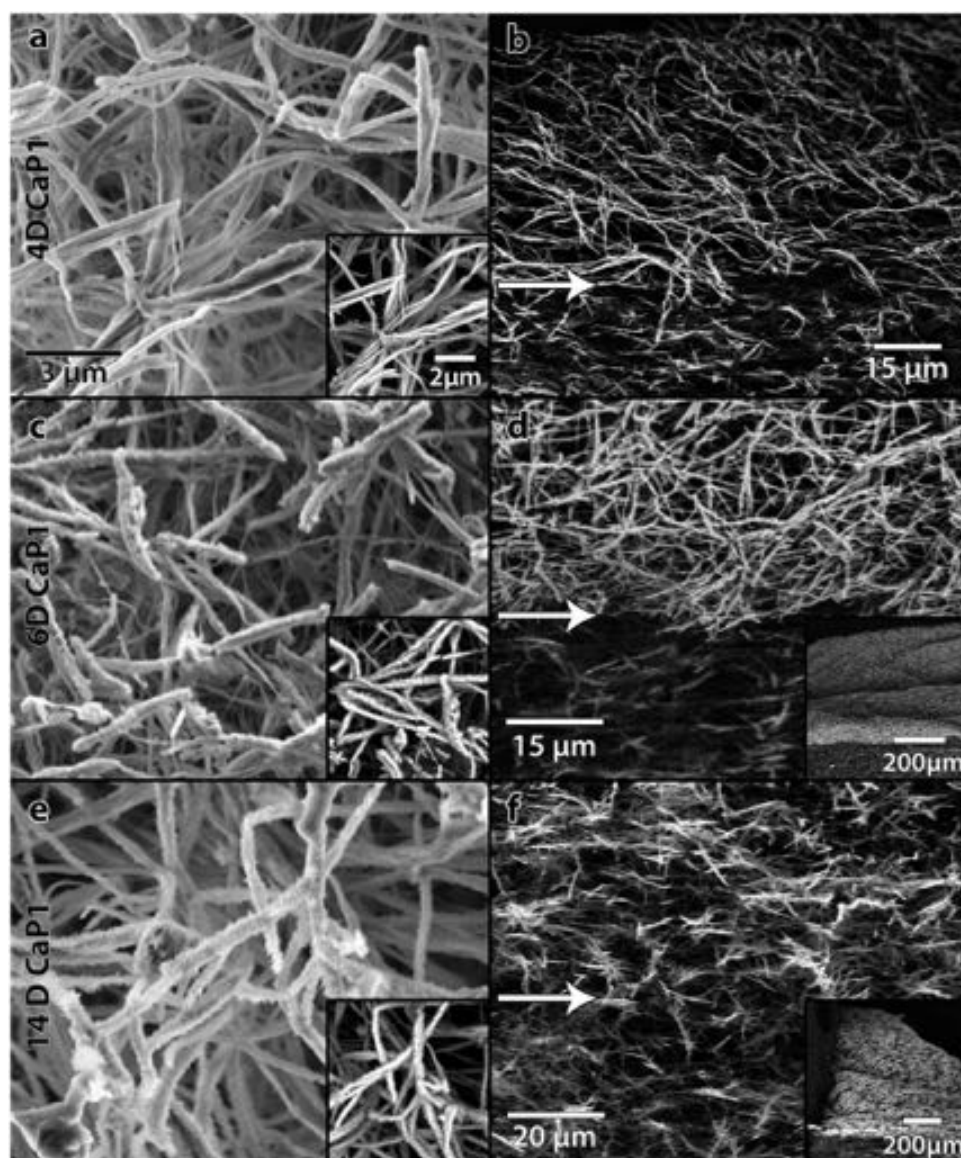


Figure 5. SEM micrographs showing the development of a hypermineralized layer over 4, 6, and 14 d of mineralization. Left-hand images ((a), (c), and (e)) are secondary electron images showing the morphology of the top surface of the scaffold (insets show BSE). At 6 d we start to see some extrafibrillar mineral, evidenced by the development of a spiky morphology on mineralized fibrils. No mineral is seen between fibrils even at 14 d. Right-hand images ((b), (d), and (f)) show BSE of the interface between the hypermineralized layer and the bulk (cross-section). Insets are lower magnification to show thickness of the hypermineralized layer. We note that (b) has no inset since the full thickness is apparent. Thickness increases over time from $\approx 60 \mu\text{m}$ to over $\approx 700 \mu\text{m}$ by 14 d. The border between the hypermineralized layer and the bulk is sharp and well defined, as indicated by arrows.

interfaces. Specifically, we designed a trilayered scaffold that resembles the periodontium, the set of tissues (bone, ligament, and cementum), which is responsible for tooth attachment. Our well-plate mineralization system gives us spatial control over mineralization, as well as control over the number of layers and their thicknesses, allowing us to tailor individual compartments for the regeneration of specific tissues. The mineralized collagen itself closely mimics native mineralized collagen fibrils, a feature which has been shown to promote cell differentiation and bone formation.^[45,46] Further, our scaffolds have intrinsic connectivity and porosity, allowing us to combine any number of layers together with no need for adhesives or other techniques. These scaffolds are potentially suited for any

hard–soft tissue interface such as tendon entheses, ligament insertions, osteochondral zones, or the periodontium.

Creating fully mineralized collagen scaffolds is inherently challenging due to diffusional limitations, which often result in significant surface mineralization. Not surprisingly, surface mineralization slows or eliminates mineralization in the bulk.^[48,49,58] Wang et al. showed an $\approx 15 \mu\text{m}$ thick mineral layer on the surface of a mineralizing tissue-like collagen matrix.^[48] This layer was nonporous and inhibited diffusion of ions into the bulk of the collagen matrix. Li et al. have been successful in creating $100 \mu\text{m}$ thick fully mineralized scaffolds, but larger scaffolds still present a challenge.^[36] An advantage of our in-well mineralization system is the ease of analyzing mineral

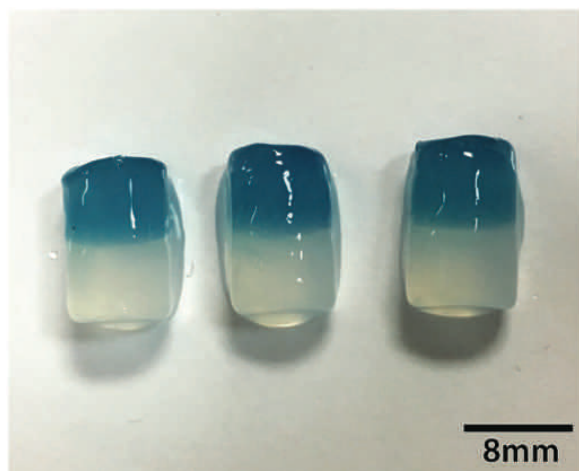


Figure 6. Optical image of bilayer collagen gels indicating the sharp interface and connection between layers. Blue layer contains Alcian blue.

distribution, as a function of depth (from the surface). We expected that our system would result in a gradient of mineralization, with the maximum amount being found on the surface (which directly contacts the mineralization solution). Instead, we see the formation of a hypermineralized surface

layer, below which the bulk seems to mineralize homogeneously, albeit at a slower rate. Since the mineral predominantly forms in the intrafibrillar space, the scaffold remains porous, allowing diffusion of ions into the scaffold freely. This allows the full thickness (≈ 2 mm) of the scaffold to mineralize, an important aspect when creating scaffolds for bone regeneration.

Hypermineralization of the surface layer could be explained by the formation of calcium phosphate aggregates, which are known to form in solutions with pAsp,^[59] as shown schematically in **Figure 9**. This amorphous phase (possibly a polymer induced liquid precursor phase^[39]) diffuses more slowly than free pAsp and $\text{Ca}^{2+}/\text{PO}_4^{3-}$ ions, and thus will contribute directly to the intrafibrillar mineralization of the surface. Meanwhile, free (nonaggregated) pAsp and $\text{Ca}^{2+}/\text{PO}_4^{3-}$ ions diffuse into the bulk of the scaffold and form aggregates, which results in intrafibrillar mineralization of the bulk. This could explain why the rate of mineralization at the surface layer is much faster than the bulk, as the precipitation of a mineral phase within the bulk gel will reduce calcium and phosphate concentrations, which are limited by diffusion. This is supported by the work of Olszta et al. who looked at the diffusion of fluorescently labeled pAsp into tendon.^[39] They found pAsp penetration depths greater than 500 μm , after which there was a sharp “falloff” in intensity. We observe a similar effect in mineralization depth

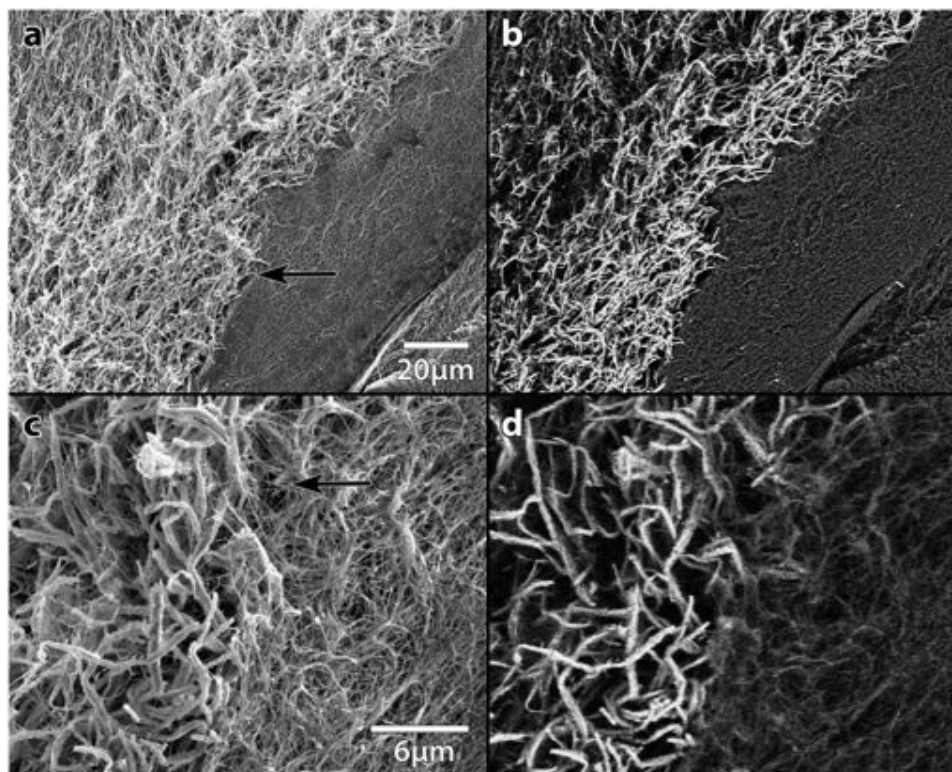


Figure 7. SEM micrographs of a biphasic collagen scaffold with a mineralized layer (6 d) and an unmineralized layer by both secondary (left) and BSE (right) imaging (cross-section). a) The sharp interface between the layers, indicated by the arrow. We note that the collagen density is the same in both layers; the appearance that the unmineralized layer is less dense is an artifact of lyophilization. b) The mineral distribution, which is restricted to the mineralized compartment. c) A higher magnification of the same area. Unmineralized fibrils are seen inserting into the mineralized layer creating mechanical interlock. The scaffold remains continuous and interconnected between layers. (d) emphasizes how sharp the interface is and confirms that mineral is restricted to the one layer.

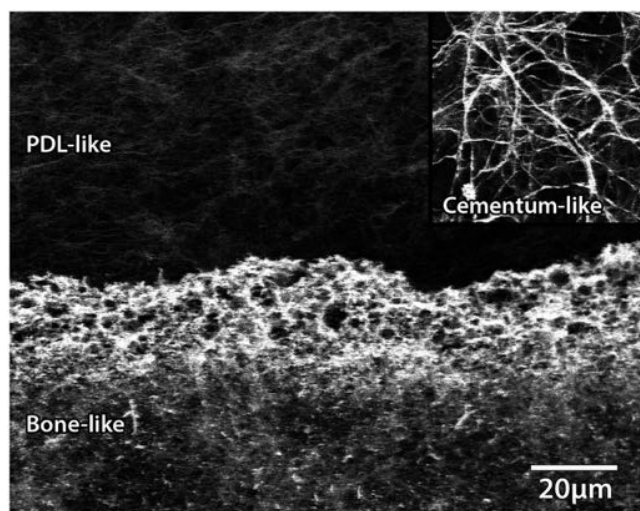


Figure 8. BSE micrograph of a triphasic collagen scaffold resembling the periodontium. The interface between the premineralized bone compartment and the unmineralized periodontal ligament compartment is shown (cross-section). The inset shows the presence of a thin mineralized layer on the top of the PDL compartment for the regeneration of cementum (top view). The bone compartment was mineralized for 10 d and the cementum compartment for 4 d.

of the hypermineralized layer, where there is a sharp interface between the hypermineralized layer and the bulk.

Our novel fabrication system enables us to create layered mineralized–unmineralized constructs. Taking advantage of the in-well mineralization system we can incorporate additional layers by pipetting new acid soluble collagen onto premineralized gels and slowly raising the pH. This method is similar to the work of Al-Munajjed et al.^[28] and Levingstone et al.^[1] who

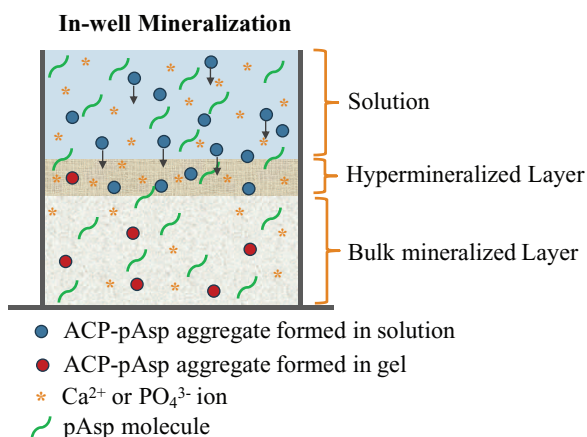


Figure 9. Schematic showing the proposed mechanism for the formation of a hypermineralized layer in mineralizing collagen gels. Calcium and phosphate ions form amorphous aggregates with pAsp in solution, which result in the intrafibrillar mineralization of the surface. These aggregates slow to diffuse into the gel. Nonaggregated ions and pAsp molecules diffuse into the bulk, and form aggregates from within the gel, resulting in bulk mineralization (intrafibrillar). However, ion depletion results in a slower mineralization than on the surface. These two mechanisms result in two rates of mineralization.

use collagen slurries that are frozen and lyophilized together to create multilayered constructs, which may be interconnected (not well characterized). However, the structure and mineral phase poorly reflect native tissues. Using our system, adjacent layers have inherent connectivity and continuous porosity that adhere together by mechanical interlock. Presumably, when acid soluble collagen is added to the well, it begins to diffuse into the first layer. Mineral dissolution during this time seems minimal. As the pH begins to rise as a result of the ammonia atmosphere, the collagen begins to self-assemble, forming fibrils that traverse the interface between the two layers. The connection between layers is not noticeably weaker than the bulk scaffold itself and does not break preferentially at the interface. This allows for intimately associated layers with intrinsic connectivity and maintained porosity, with no need for adhesives or heat treatments.

Incorporating layers using buffer neutralization (rather than ammonia neutralization) will make this system compatible with cell, vector, and growth factor delivery, allowing for layers to be gelled together, preseeded with the appropriate molecule and/or cell populations. This has the potential to simplify manufacturing techniques. However, the rate of gelation is an important factor in interlayer cohesion; faster gelling techniques may make cohesion more difficult to achieve. As such control over the rate of buffer neutralization would be necessary. Similarly, pore sizes could be tailored for specific cell populations relevant to the specific layer using different porogens.

The development of a hypermineralized layer in our system allows for the production of thin mineralized layers. In doing so, we can create trilayered structures that incorporate two mineralized compartments surrounding an unmineralized inner compartment. Such scaffolds are particularly well suited to periodontal regeneration, as the periodontium consists of bone, periodontal ligament, and cementum, a thin mineralized tissue contacting the tooth root. Such scaffolds can mimic the complicated architecture of the periodontium and provide appropriate mechanical properties to help guide hard and soft tissue regeneration. This system can also be used to create scaffolds tailored to other purposes such as osteochondral defects. The incorporation of mineralization proteins or peptides to the bone and cementum compartments could be used to gain further spatial control over mineralization. Additionally, possible incorporation of specific cells, growth factors, and/or vectors could further promote tissue regeneration in each compartment.

4. Conclusions

Here we show a trilayered scaffold resembling the periodontium, which incorporates individual compartments for the regeneration of bone, periodontal ligament, and cementum. The in-well mineralization/assembly system described allows for the creation of successive layers that incorporate biomimetic mineralization and potentially other desired additives into specific layers. Further, the system results in intrinsic cohesion between layers, and does not require adhesives or other treatments to maintain the integrity of the scaffold. In the future this system can be made compatible with cell, peptide, growth factor, or gene delivery. Although this work is inspired by the

periodontium, this approach is well suited for any tissue interface and has the potential to improve therapeutic outcomes for a variety of tissue regeneration applications.

5. Experimental Section

All chemicals were purchased from Sigma-Aldrich (Oakville, ON, Canada) unless otherwise specified. Water used in experiments was either distilled (dH₂O) or deionized (Milli-Q; Millipore, USA). Rat tail tendons were donated from other labs after the sacrifice of control animals. All animal protocols for the collection of rat tails were approved by the Animal Care Committee at the University of Toronto and conducted according to their guidelines.

Collagen Extraction and Purification: Type I collagen was extracted from rat tail tendons via acid dissolution. All reagents, tools, and vessels were autoclaved prior to the procedure. Briefly, rat tail tendons were surgically extracted from rat tails using bone snips and surgical scissors in a sterile, laminar flow hood. Tendons were washed in 50 mL conical tubes by centrifugation at 5500 rpm at 4 °C for 5 min to pellet the tendons. Washing was done in phosphate buffered saline (Dulbecco's 1X phosphate buffered saline (PBS), three times) followed by 4 M NaCl, and PBS again (three times). Tails were then dissolved in 0.5 M acetic acid (Caledon Laboratory Chemicals, ON, CAN) at ≈ 75 mL per tail for 24 h at 4 °C. The resulting viscous solution was centrifuged at 14 000 rpm and 4 °C for 120 min. The supernatant was collected and reprecipitated by adding 4 M NaCl to a final concentration of $\approx 700 \times 10^{-3}$ M NaCl. Reprecipitation was allowed to occur for >4 h, stirred. The collagen was then centrifuged for 15 min at 6000 rpm and 4 °C to collect the precipitated collagen (pellet). The precipitate was redissolved in 0.5 M acetic acid overnight (≈ 1.8 L acid/200 g pellet). The resulting solution was dialyzed against 50×10^{-3} M acetic acid over 3 d to remove salt, changing the dialysate regularly. The purified collagen solution was then centrifuged at 14 000 rpm and 4 °C for 120 min to remove any undissolved collagen. Collagen solution was then transferred to 50 mL conical tubes and lyophilized. Lyophilized collagen was stored at -20 °C and redissolved in acetic acid to desired concentrations.

Scaffold Manufacturing: Collagen scaffolds were produced by gel casting in 24 or 96-well plates (Sarstedt, DK). Briefly, collagen was dissolved in 0.5 M acetic acid at 3 mg mL⁻¹. Collagen solution was degassed under vacuum until no bubbles were visible (≈ 30 min) and cooled to 4 °C. Acid soluble collagen was pipetted into each well. Volumes were chosen based on the application and the size of well. Plates were placed in an ammonia environment for 30–45 min for gelation to occur. Collagen gels were washed extensively (>24 h) in dH₂O to remove ammonium hydroxide. Gels were fixed by with 0.6% glutaraldehyde for 0.5–1 h or with a ten times molar excess of EDC in 0.1 M 2-(N-morpholino)ethanesulfonic acid (Cova Chem, USA) with 75×10^{-3} M NaCl and pH 4.5 overnight. After fixation, gels were washed extensively in dH₂O (24–48 h) to remove excess fixative. Mineralization was done using a previously reported mineralization solution^[41] containing 125 μ g mL⁻¹ polyaspartic acid (molecular weight = 14 kDa, Alamanda Polymers, AL, USA) and buffered to pH 7.4 at 37 °C with 50×10^{-3} M Tris. Ion concentrations were as follows: 133×10^{-3} M Na⁺, 2.5×10^{-3} M K⁺, 1.7×10^{-3} M Ca²⁺, 123×10^{-3} M Cl⁻, and 9.1×10^{-3} M P_i. Mineralization solution was filtered through 0.2 μ m syringe filters prior to use. Gels were mineralized on a rocker at 37 °C (for agitation) and 100% relative humidity. Mineralization solution was changed often during the first 24 h and every 1–2 d thereafter. After mineralization, gels were washed extensively to remove salts. Gels were frozen in-well, in a dry ice, 2-propanol bath (-80 °C) and then transferred to liquid nitrogen. Frozen gels were lyophilized overnight.

Adding Layers: To incorporate additional layers, acid soluble collagen was gelled in contact with first layer, which could be mineralized or unmineralized. Ammonium hydroxide was pipetted into interwell spaces or adjacent empty wells prior to pipetting second layer. Acid soluble collagen (3 mg mL⁻¹, 0.5 M acetic acid) was pipetting to desired

thickness onto first layer. The lid was parafilmed in place, allowing for a space above the wells between the lid to allow gas diffusion. Collagen was gelled in the ammonia atmosphere for 30–45 min. Plates were washed copiously in distilled water. The second layer was fixed in 0.6% glutaraldehyde for 10 min. Gels were washed extensively again in distilled water for at least 24 h.

Electron Microscopy: For SEM, lyophilized scaffolds were mounted on aluminum stubs with carbon tape and coated with a visible thickness of carbon. Imaging was done on a Hitachi SU3500 SEM with a backscattered electron detector. Imaging was done at 5 kV, using aperture 3 and a spot size of 35. EDX was performed on an Oxford Instruments, 80 mm square EDS X-Max Detector, with the AZtec software package.

For TEM, hydrated scaffolds were homogenized with a razor blade. Scaffold homogenate was incubated on nickel TEM grids supported with carbon-coated formvar for 2 min to allow collagen fibrils to adhere. Excess material and water was wicked away and grids were air dried and stored for analysis. Imaging was done on an FEI Tecnai 20 TEM with an AMT 1600 side mount camera operating at 200 kV. Uranyl acetate staining was done by incubating grids on two changes of Milli-Q followed by two changes of 2% uranyl acetate followed by a 5 min staining period. Grids were washed through three changes of Milli-Q water, air dried, and stored for imaging.

Thermogravimetric Analysis: For TGA, samples were washed to remove excess salts and lyophilized. TGA was done on a TA Instruments Q500. Samples were heated to under air from room temperature to 105 °C where the temperature was held for 5 min to remove residual water. Sample temperature was then ramped to 700 °C. The mass at 660 °C was taken as the total inorganic mass.^[36] Weight percent of mineral was compared between EDC and glutaraldehyde-fixed scaffolds ($n = 3$). Significance was determined by 1-way ANOVA analysis with a Tukey post hoc test ($\alpha = 0.05$).

Supporting Information

Supporting Information is available from the Wiley Online Library or from the author.

Acknowledgements

This research was supported by a Canadian Institutes of Health Research Operating Grant (MOP-14273) and a Natural Sciences and Engineering Research Council of Canada (NSERC) Discovery Grant to E.D.S. A.J.L. is grateful to the NSERC CREATE Program in Regenerative Medicine for a doctoral fellowship. TEM was performed at the Advanced Bioimaging Center at Sick Kids Hospital in Toronto, Canada. SEM was performed at the Ontario Centre for the Characterisation of Advanced Materials (OCCAM) in the Department of Material Science and Engineering at the University of Toronto.

Conflict of Interest

The authors declare no conflict of interest.

Keywords

biomimetic materials, biomineralization, intrafibrillar hydroxyapatite, layered scaffolds, periodontium

Received: July 10, 2018
Revised: August 24, 2018
Published online:

- [1] T. J. Levingstone, A. Matsiko, G. R. Dickson, F. J. O'Brien, J. P. Gleeson, *Acta Biomater.* **2014**, *10*, 1996.
- [2] S. Saha, B. Kundu, J. Kirkham, D. Wood, S. C. Kundu, X. B. Yang, *PLoS One* **2013**, *8*, e80004.
- [3] P.-A. Mouthuy, Y. El-Sherbini, Z. Cui, H. Ye, *J. Tissue Eng. Regener. Med.* **2016**, *10*, E263.
- [4] E. Kon, M. Delcogliano, G. Filardo, M. Fini, G. Giavaresi, S. Francioli, I. Martin, D. Pressato, E. Arcangeli, R. Quarto, M. Sandri, M. Marcacci, *J. Orthop. Res.* **2010**, *28*, 116.
- [5] W. Swieszkowski, B. H. S. Tuan, K. J. Kurzydowski, D. W. Hutmacher, *Biomol. Eng.* **2007**, *24*, 489.
- [6] S. Ivanovski, C. Vaquette, S. Gronthos, D. W. Hutmacher, P. M. Bartold, *J. Dent. Res.* **2014**, *93*, 1212.
- [7] J. E. Jeon, C. Vaquette, C. Theodoropoulos, T. J. Klein, D. W. Hutmacher, *J. R. Soc. Interface* **2014**, *11*, 20140184.
- [8] J. P. Spalazzi, M. C. Vyner, M. T. Jacobs, K. L. Moffat, H. H. Lu, *Clin. Orthop. Relat. Res.* **2008**, *466*, 1938.
- [9] J. P. Spalazzi, S. B. Doty, K. L. Moffat, W. N. Levine, H. H. Lu, *Tissue Eng.* **2006**, *12*, 3497.
- [10] J. E. Phillips, K. L. Burns, J. M. Le Doux, R. E. Guldberg, A. J. García, *Proc. Natl. Acad. Sci. USA* **2008**, *105*, 12170.
- [11] N. H. Dormer, C. J. Berkland, M. S. Detamore, *Ann. Biomed. Eng.* **2010**, *38*, 2121.
- [12] A.-M. Yousefi, M. E. Hoque, R. G. S. V. Prasad, N. Uth, *J. Biomed. Mater. Res., Part A* **2015**, *103*, 2460.
- [13] H. H. Lu, S. Thomopoulos, *Annu. Rev. Biomed. Eng.* **2013**, *15*, 201.
- [14] H. H. Lu, S. D. Subramony, M. K. Boushell, X. Zhang, *Ann. Biomed. Eng.* **2010**, *38*, 2142.
- [15] M. Singh, C. Berkland, M. S. Detamore, *Tissue Eng., Part B* **2008**, *14*, 341.
- [16] E. Kon, G. Filardo, F. Perdisa, G. Venieri, M. Marcacci, *J. Exp. Orthop.* **2014**, *1*, 1.
- [17] P. M. Bartold, C. A. G. McCulloch, A. S. Narayanan, S. Pitaru, *Periodontol. 2000* **2000**, *24*, 253.
- [18] C. H. Park, H. F. Rios, Q. Jin, M. E. Bland, C. L. Flanagan, S. J. Hollister, W. V. Giannobile, *Biomaterials* **2010**, *31*, 5945.
- [19] E. C. Carlo Reis, A. P. B. Borges, M. V. F. Araújo, V. C. Mendes, L. Guan, J. E. Davies, *Biomaterials* **2011**, *32*, 9244.
- [20] C. H. Park, H. F. Rios, Q. Jin, J. V. Sugai, M. Padial-Molina, A. D. Taut, C. L. Flanagan, S. J. Hollister, W. V. Giannobile, *Biomaterials* **2012**, *33*, 137.
- [21] C. Vaquette, W. Fan, Y. Xiao, S. Hamlet, D. W. Hutmacher, S. Ivanovski, *Biomaterials* **2012**, *33*, 5560.
- [22] C. H. Lee, J. Hajibandeh, T. Suzuki, A. Fan, P. Shang, J. J. Mao, *Tissue Eng., Part A* **2014**, *20*, 1342.
- [23] E. M. Varoni, S. Vijayakumar, E. Canciani, A. Cochis, L. De Nardo, G. Lodi, L. Rimondini, M. Cerruti, *J. Dent. Res.* **2018**, *97*, 303.
- [24] P. F. Costa, C. Vaquette, Q. Zhang, R. L. Reis, S. Ivanovski, D. W. Hutmacher, *J. Clin. Periodontol.* **2014**, *41*, 283.
- [25] M. Mizuno, R. Fujisawa, Y. Kuboki, *J. Cell. Physiol.* **2000**, *184*, 207.
- [26] M. Mizuno, Y. Kuboki, *J. Biochem.* **2001**, *129*, 133.
- [27] G. Xiao, D. Wang, M. D. Benson, G. Karsenty, R. T. Franceschi, *J. Biol. Chem.* **1998**, *273*, 32988.
- [28] A. A. Al-Munajjed, N. A. Plunkett, J. P. Gleeson, T. Weber, C. Jungreuthmayer, T. Levingstone, J. Hammer, F. J. O'Brien, *J. Biomed. Mater. Res., Part B* **2009**, *90B*, 584.
- [29] G. Wang, M. E. Babadağlı, H. Uludağ, *Mol. Pharm.* **2011**, *8*, 1025.
- [30] A. Sionkowska, J. Kozłowska, *Int. J. Biol. Macromol.* **2013**, *52*, 250.
- [31] M. S. Islam, M. Todo, *Mater. Lett.* **2016**, *173*, 231.
- [32] R. Cholas, S. Kunjalukkal Padmanabhan, F. Gervaso, G. Udayan, G. Monaco, A. Sannino, A. Licciulli, *Mater. Sci. Eng. C* **2016**, *63*, 499.
- [33] R. J. Kane, R. K. Roeder, *J. Mech. Behav. Biomed. Mater.* **2012**, *7*, 41.
- [34] L. J. Smith, A. C. Deymier, J. J. Boyle, Z. Li, S. W. Linderman, J. D. Pasteris, Y. Xia, G. M. Genin, S. Thomopoulos, *Interface Focus* **2016**, *6*, 20150070.
- [35] D. W. Weisgerber, D. O. Kelkhoff, S. R. Caliar, B. A. C. Harley, *J. Mech. Behav. Biomed. Mater.* **2013**, *28*, 26.
- [36] Y. Li, T. T. Thula, S. Jee, S. L. Perkins, C. Aparicio, E. P. Douglas, L. B. Gower, *Biomacromolecules* **2012**, *13*, 49.
- [37] D. W. Weisgerber, S. R. Caliar, B. A. C. Harley, *Biomater. Sci.* **2015**, *3*, 533.
- [38] J. C. Lee, C. T. Pereira, X. Ren, W. Huang, D. Bischoff, D. W. Weisgerber, D. T. Yamaguchi, B. A. Harley, T. A. Miller, *J. Craniofac. Surg.* **2015**, *26*, 1992.
- [39] M. J. Olszta, X. Cheng, S. S. Jee, R. Kumar, Y. Y. Kim, M. J. Kaufman, E. P. Douglas, L. B. Gower, *Mat. Sci. Eng. R* **2007**, *58*, 77.
- [40] F. Nudelman, K. Pieterse, A. George, P. H. Bomans, H. Friedrich, L. J. Brylka, P. A. Hilbers, G. de With, N. A. Sommerdijk, *Nat. Mater.* **2010**, *9*, 1004.
- [41] A. J. Lausch, B. D. Quan, J. W. Miklas, E. D. Sone, *Adv. Funct. Mater.* **2013**, *23*, 4906.
- [42] A. S. Deshpande, E. Beniash, *Cryst. Growth Des.* **2008**, *8*, 3084.
- [43] Y. Liu, Y. K. Kim, L. Dai, N. Li, S. O. Khan, D. H. Pashley, F. R. Tay, *Biomaterials* **2011**, *32*, 1291.
- [44] L.-N. Niu, S. E. Jee, K. Jiao, L. Tonggu, M. Li, L. Wang, Y.-D. Yang, J.-H. Bian, L. Breschi, S. S. Jang, J.-H. Chen, D. H. Pashley, F. R. Tay, *Nat. Mater.* **2017**, *16*, 370.
- [45] Y. Wang, N. Van Manh, H. Wang, X. Zhong, X. Zhang, C. Li, *Int. J. Nanomed.* **2016**, *11*, 2053.
- [46] Y. Liu, D. Luo, X.-X. Kou, X.-D. Wang, F. R. Tay, Y.-L. Sha, Y.-H. Gan, Y.-H. Zhou, *Adv. Funct. Mater.* **2013**, *23*, 1404.
- [47] B. Ye, X. Luo, Z. Li, C. Zhuang, L. Li, L. Lu, S. Ding, J. Tian, C. Zhou, *Mater. Sci. Eng. C* **2016**, *68*, 43.
- [48] Y. Wang, T. Azaïs, M. Robin, A. Vallée, C. Catania, P. Legriel, G. Pehau-Arnudet, F. Babonneau, M. M. Giraud-Guille, N. Nassif, *Nat. Mater.* **2012**, *11*, 724.
- [49] T. T. Thula, D. E. Rodriguez, M. H. Lee, L. Pendi, J. Podschun, L. B. Gower, *Acta Biomater.* **2011**, *7*, 3158.
- [50] T. T. Thula, D. E. Rodriguez, M. H. Lee, L. Pendi, J. Podschun, L. B. Gower, *Acta Biomater.* **2011**, *7*, 3158.
- [51] V. K. Selestina Gorgieva, in *Biomaterials Applications for Nanomedicine* (Ed: R. Pignatello), InTech, Rijeka, Croatia **2011**, pp. 17–52.
- [52] P. N. Jones, *Connect. Tissue Res.* **1991**, *26*, 11.
- [53] J. A. Chapman, M. Tzaphlidou, K. M. Meek, K. E. Kadler, *Electron Microsc. Rev.* **1990**, *3*, 143.
- [54] A. J. Lausch, E. D. Sone, *Biomacromolecules* **2015**, *16*, 1938.
- [55] W. Traub, T. Arad, S. Weiner, *Proc. Natl. Acad. Sci. USA* **1989**, *86*, 9822.
- [56] B. D. Quan, E. D. Sone, *Bone* **2015**, *77*, 42.
- [57] E. Beniash, *WIREs Nanomed. Nanobiotechnol.* **2011**, *3*, 47.
- [58] T. T. Thula, F. Svedlund, D. E. Rodriguez, J. Podschun, L. Pendi, L. B. Gower, *Polymers* **2011**, *3*, 10.
- [59] D. V. Krogstad, D. Wang, S. Lin-Gibson, *Biomacromolecules* **2015**, *16*, 1550.